Arch. Metall. Mater. **65** (2020), 1, 55-64

DOI: 10.24425/amm.2019.131096

M. KORALNIK[1*], A. DOBKOWSKA[1,2], B. ADAMCZYK-CIESLAK[1], J. MIZERA[1]

THE INFLUENCE OF THE MICROSTRUCTURAL EVOLUTION ON THE CORROSION RESISTANCE OF COLD DRAWN COPPER SINGLE CRYSTALS IN NaCl

The aim of the present work was to determine the influence of the microstructural evolution of copper single crystals with the initial orientations of <001> and <111> after cold drawing on their corrosion resistance. Transmission electron microscopy, X-ray diffraction, and electron backscattering diffraction were used to characterize the microstructural changes. To evaluate the corrosion resistance after deformation, open circuit potential, electrochemical impedance spectroscopy, and potentiodynamic polarization analyses were conducted. The microstructural observations showed the presence of dislocation cell structures and shear bands in deformed sample with initial orientation <001> single crystal, as well as a strongly-developed substructure in sample <111>. The material with initial orientation of <001> was more resistive in analyzed medium than material with the initial orientation of <111>.

Keywords: copper single crystal, microstructure and texture evolution, impedance spectroscopy, potentiodynamic polarization, open circuit potential

1. Introduction

The corrosion resistance of all structural materials is strongly-dependent on the microstructure and texture evolution. Recently, cold drawing has become one of the most common methods to deform commercially-used pure Cu [1] by deforming fcc metals to create ultrafine or even nano-sized microstructure [2]. A detailed description of the microstructure and texture evolution of cold drawn Cu single crystals as a function of their initial <111> and <100> orientations was made by Chen et al. [3]. The authors showed that in cold drawn Cu, the initial orientation was an important factor affecting the fiber texture ratio of <111> to <100>. The development of texture deformation during Cu wire drawing has also been described for all three principal directions (radial (*R*), tangential (*T*), and axial (*A*)) by Rajan et al. [4], who investigated cold drawn Cu wire with a 93% diameter reduction. They examined the stereographic inverse pole figure (IPF), which revealed the crystallographic IPF for each principal direction. The study showed that a double fiber texture of <111> and <100> formed parallel to the axis direction. Similar results were obtained for Ag, where the double fiber texture of <111> and <100> parallel to the axis direction was also defined after drawing 13 mm rods to diameter 8.85 mm [5]. The ratio of the above mentioned texture components of deformed fcc materials is strongly related to several factors, including the stacking fault energy (SFE) of materials [6,7]. Metals with high SFE exhibit principal <111> fiber, and as the SFE decreases, the fraction of the <100> component increases [8]. The deformation rate and temperature of deformation strongly influence the final texture formation for cold rolling textures of fcc materials as well [9,10].

The development of deformation texture during the drawing process of fcc metals has already been examined, but there is no indication as to how the texture formation after subsequent plastic deformation of Cu single crystals with different initial orientations impacts the corrosion properties. Knowing that the crystallographic orientation can influence the dissolution rate of susceptible areas in Cu [11], it is desirable to define the electrochemical behavior of cold drawn Cu. It has been shown that uniform copper corrosion can occur in solutions with low pH and high alkalinity [12,13]. In neutral conditions, the corrosion products can form an adhesive and uniform film on the copper surface, which plays a crucial role in substrate protection [14-17]. This oxide film mainly consists of cuprite (Cu_2O), tenorite (CuO), or $Cu(OH)_2$ [18]. It should be mentioned that in chloride solutions, the corrosion potential of copper and the extent of the passive zone decrease as both the temperature and

[1] WARSAW UNIVERSITY OF TECHNOLOGY, FACULTY OF MATERIALS SCIENCE AND ENGINEERING, 141 WOLOSKA ST., 02-507 WARSZAWA, POLAND
[2] WESTERN UNIVERSITY OF ONTARIO, CHEMISTRY DEPARTMENT, LONDON, CANADA

* Corresponding author: milena.koralnik.dokt@pw.edu.pl

chloride concentration increase [19]. In this type of solution, the formation of soluble $CuCl_2^-$ complexes and non-protecting CuCl can decrease the stability region of Cu_2O and CuO [18,20]. In addition, the most common metallurgical factors such as grain size distribution [21] and the corrosion of polycrystalline Cu and its alloys, are also strongly correlated with the type of grain boundary [22,23] and grains disorientations [11]. The corrosion behavior of polycrystalline Cu has also been studied in terms of its susceptibility to intergranular corrosion [24]. The authors showed that the corrosion of pure Cu produced by the Bridgman method is strongly influenced by the geometric criteria of the grain boundaries. In other studies, the crystal-orientation-dependent corrosion behavior of single crystals of different materials has been reported [25-27]. Nevertheless, there is a lack of information regarding the corrosion behavior of pure Cu as a function of its various initial single crystal orientations.

Thus, the goal of present work was to investigate the texture development of cold drawn Cu single crystals as a function of their initial orientations, <111> and <001>. In addition, the way in which the formation of the final microstructure and texture after a subsequent cold drawing process influences their corrosion resistance in a chloride-containing solution was also investigated.

2. Materials and methodology

Copper single crystals of 99.9% purity with an initial orientation of <001> and <111> were produced by a modified Bridgman method and then subjected to a cold drawing process. Plastic deformation was performed in the direction parallel to the single crystals' orientation at ambient temperature. After the two drawing passes, the material diameter was reduced from 9 mm to 3 mm, which corresponds to a total strain $\varepsilon \approx 2.2$. For the purpose of this work, the deformed material with the initial single crystal orientation <111> was marked Cu <111>, and the material with an initial orientation of <001> after drawing was marked Cu <001>.

Materials microstructures were examined using a transmission electron microscope (TEM) JEOL JEM-1200EX with an acceleration voltage of 120 kV. Thin foils of TEM samples were prepared from 3 mm diameter discs, which were cut out from the drawn Cu rods perpendicularly to the plastic deformation direction. The discs were mechanically sanded to 120 μm thickness and then electropolished at a voltage of 7 V for about 50 seconds at 0°C, using a Struers electrolyte based on phosphoric acid. According to the described samples preparation procedure, the microstructure observations in the central part of sections perpendicular to the drawing direction (DD) were carried out.

Electron backscattering diffraction (EBSD) analysis was performed using a Hitachi SU70 scanning electron microscope (SEM) on the same samples which were prepared for TEM observations. EBSD maps were registered at an acceleration voltage of 20 kV with a working distance of 18 mm and a sample tilt angle of 70°; for detailed mapping, a 0.2 μm step size was used. For each pattern, either five or six Kikuchi bands were used for indexing, minimizing the possibility of mis-indexing errors. The fraction of successfully indexed orientations for each registered map was higher than 95%, and data were analyzed using Channel5 software.

X-ray diffraction (XRD) was used to estimate the dislocation density. Based on the changes in the Bragg angle, the full width at half maximum of the diffraction peaks, and crystallite size, the dislocation density ρ can by calculated by the following equations Eq. 1-2 [28-30]:

$$\beta \cos\theta / \lambda = 0.9 / D + 2\varepsilon \sin\theta / \lambda \quad (1)$$

$$\rho = 14.4\varepsilon^2 / b^2 \quad (2)$$

where β is the peak width at half maximum in rad, θ is the Bragg angle, λ is the wavelength of the X-ray beam Cu Kα (Kα1 = 0.1542 nm), D is the crystallite size, ε is the lattice strain, ρ is the dislocation density, and b is the Burgers vector (b_{Cu} = 0.256 nm [31]).

Global texture investigations were performed using a Bruker D8 X-ray diffractometer applying filtered radiation Co Kα (Kα1 = 0.1789 nm). Deformed texture was measured over an area of approximately 1.5 mm^2 (the beam diameter was 1 mm) in the center of the sample on the cross-section in the deformation direction. Measurements were recorded within a 5° × 5° mesh and a beam intensity at 5-second intervals. Four incomplete X-ray pole figures ({111}, {200}, {220} and {311}) were used to evaluate complete orientation distribution functions (ODFs) by the spherical harmonics method and the Gauss model functions proposed by the Schultz reflection method [32]. Labotex 2.1 software was used to calculate the volume fraction of the main texture components. A tolerance angle of 10° was used during the calculation of the volume fractions.

For the electrochemical tests and scanning electron microscopy surface examinations, the samples were also cut out perpendicularly to the drawing direction and prepared by grinding and then mechanically polished with a monocrystalline diamond suspension (3 and 1 μm). To determine the corrosion behavior of examined material, electrochemical tests were conducted in a neutral 3.5 wt.% water solution of sodium chloride NaCl (aerated) in ambient temperature with an Autolab PGSTAT 100 potentiostat with Nova software. Prior to electrochemical impedance spectroscopy (EIS), the corrosion potential E_{corr} evaluation in open circuit potential (OCP) was registered for 30 minutes. The EIS spectra were registered in a frequency range from 0.01 to 10^5 Hz and potentiodynamic polarization (PDP) tests with a scan rate of 0.01 V/s were also conducted. For the electrochemical tests, a traditional three-electrode setup was used, with Pt as a counter electrode and Ag/AgCl as a reference electrode. The obtained polarization data was analyzed using Nova 2.1.2 software, and the EIS results were fitted with EIS Analyzer in Powell mode. To evaluate the surface changes after corrosion tests, the SEM observations using Hitachi S3500 microscope were made with an acceleration voltage of 20 kV.

3. Results and discussion

The TEM bright field (BF) images obtained for deformed Cu single crystals with initial orientations of <111> and <001> are presented in Figs 1-2. Due to the cold drawing process, strongly developed substructure with many dislocations was obtained in both samples. Nevertheless, differences were observed in the microstructure formation depending on the materials' initial orientation. In Fig. 1a and b, weakly molded structure with locally clear grain boundaries was observed for deformed Cu <111>. It was possible to distinguish the dominant most active slip system during deformation, accordance with the direction <110> (marked by a dashed line in Fig. 1b). Based on the XRD measurements, the dislocation density calculated for this sample was about 2.35×10^{15} m^{-2}. A heterogeneous microstructure with elongated subgrains was observed for the Cu <001> (Fig. 2a). As shown in Fig. 2b, areas with dislocation cell structure were also identified. A quantitative analysis, which was performed using stereological software [33], estimated an average dislocation cell structure size of about 290 nm. Furthermore, the dislocation structure led to an increase in dislocation density to 4.06×10^{15} m^{-2} in the examined sample. The formation of dislocation cells or grain structures depends on which slip system more preferentially activates. The microstructural observations of Cu <001> show the presence of shear bands (Fig. 3a and b). The activation of the coplanar secondary slip system is present during the cell structure formation [34,35]. Due to the heterogeneous

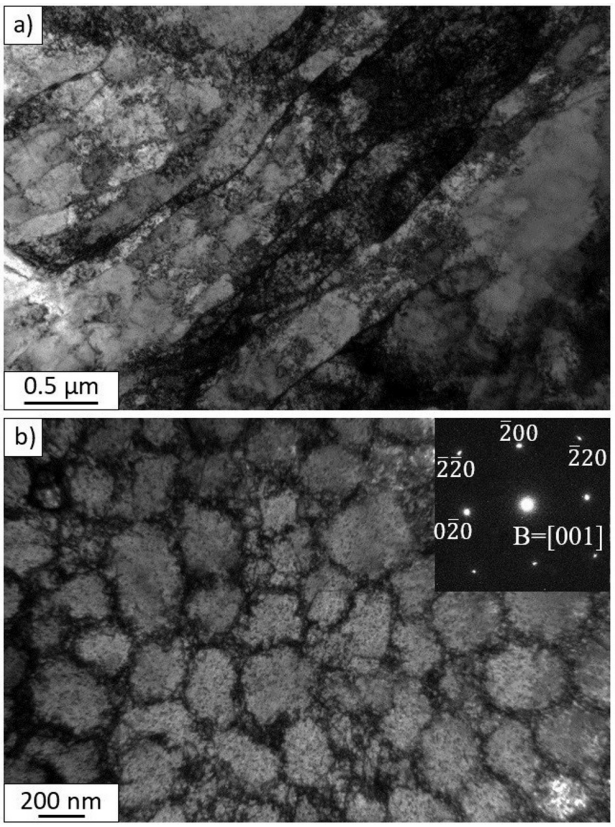

Fig. 2. TEM images of the cold drawn Cu <001>: a) representative microstructure, b) microstructure at higher magnification with diffraction pattern at the zone axis <001>

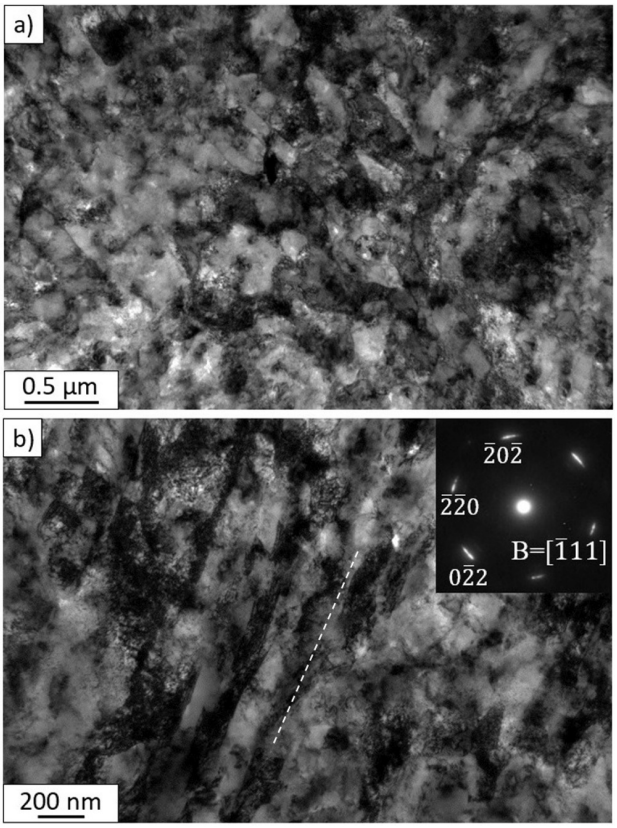

Fig. 1. TEM images of the cold drawn Cu <111>: a) representative microstructure, b) microstructure at higher magnification with diffraction pattern close to the zone axis <111>

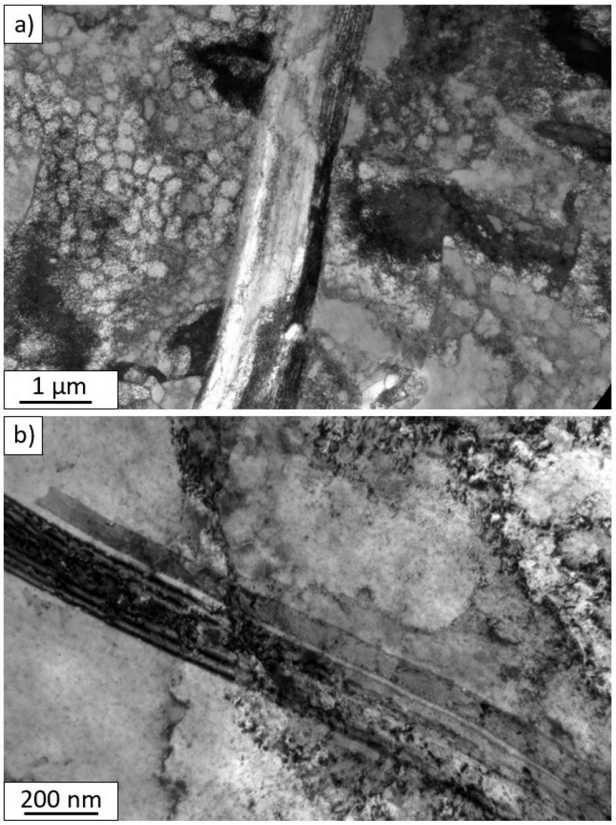

Fig. 3. The shear bands at TEM images obtained for the cold drawn Cu <001> a) at the areas of dislocation cells structure, b) at higher magnification

microstructure and the presence of dislocation cells and shear bands, for sample Cu <001> it was not possible to determine one, the most active slip system during deformation. For materials with low SFE (like Cu) shear banding is preceded by the blockage of dislocation slip at an early stage of deformation [36,37]. Dislocation cells or band-like dislocation cells, as well as high local orientation changes at the boundary between the band and the material matrix contained mechanical instabilities, which initiate the shear banding process [37,38]. The obtained results confirmed that the initiation of shear banding depends on the initial orientation of the crystals and the texture components.

The texture evolution of the investigated cold drawn copper single crystals with initial orientations of <111> and <001> was characterized by orientation distribution functions (ODFs), with sections at $\varphi_2 = 0°$ and $\varphi_2 = 45°$ (Fig. 4).

In the Cu <111> sample after deformation, the texture can be described as a fiber with a local maximum, which is close to a typical γ fiber (<111> parallel to normal direction). This type of fiber typically forms in fcc materials due to plastic deformation, as previously reported by Kestens et al. [39] and Huang et al. [40]. Besides the random texture (background is almost 60% of the volume fraction), there are two moderately strong texture components, which are {11 11 13} <$\bar{2}$ $\bar{1}\bar{1}$ 11> and {1 1 1} <$\bar{2}$ 1 1>, with volume fractions of 22% and 11%, respectively. The maxima of the first orientation are slightly deviated (≈5°) from the corresponding ideal position of <111> fiber. The reason for that, is most likely in the asymmetry flow of material during deformation. Additionally, the {1 1 1} <$\bar{2}$ 1 1> orientation is described in the literature as an F component, which is associated with the appearance of shear bands [41-43]. This phenomenon was described for austenitic steel by Odnobokova et al. [41], where shear banding was initiated by micro-shearing within a grain that and progressively propagated over neighboring grains. The microstructure observations do not clearly confirm the presence of micro-shear banding due to the strongly-developed and defective microstructure of the Cu <111> sample.

The results obtained for Cu <111> (Fig. 4a) also demonstrate the presence of local maxima, which is atypical for materials after axial deformation. This means that the texture gradient that exists in cold drawn Cu forms because of severe non-uniform deformation. In addition to the total strain, die geometry, uniform drawing forces, or friction during deformation may affect the strain path and the distribution of the texture components [44,45].

Significantly different ODFs were obtained for Cu <001> (Fig. 4b), and the developed texture was not too sharp and the <001> fiber with a local maximum corresponding to the {0 0 1} <1 2 0> component was formed. Moreover, the calculated volume fractions of the individual texture component (35% of {0 0 1} <1 2 0> orientation) and the high level of background (≈60% of the volume fraction) show that a stronger texture is formed in the Cu <111> sample than in Cu <001>. The cold drawn Cu single crystal with <001> initial orientation is also characterized by an axial texture, however, the <111> fiber, which is predominant in Cu <111> has undergone a significant broadening and weakening (up to 5% of volume fraction).

The differences between the texture orientations after deformation of copper single crystals are well represented by the inverse pole figures (IPFs) given in Fig. 4 c and d. The Cu <001> has a relatively weak texture with a dominant <001> fiber parallel to the longitudinal drawing direction. For the Cu <111> sample, a strong <111> texture component was generated during the cold drawing process.

The EBSD results obtained for Cu <111> (Fig. 5a,b) show the presence of a sharp texture around the <111> direction which is retained from the single crystal initial orientation. As

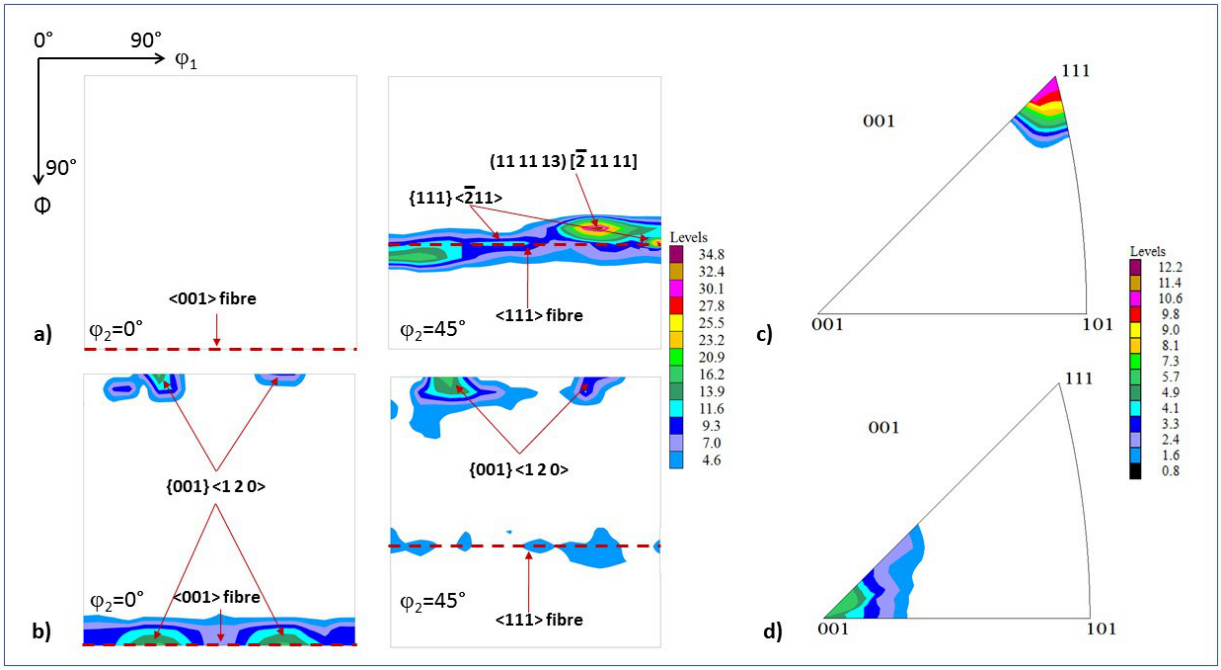

Fig. 4. The ODFs at $\varphi_2 = 0°$ and $\varphi_2 = 45°$ and IPFs for: a, c) Cu <111> and b, d) Cu <001>

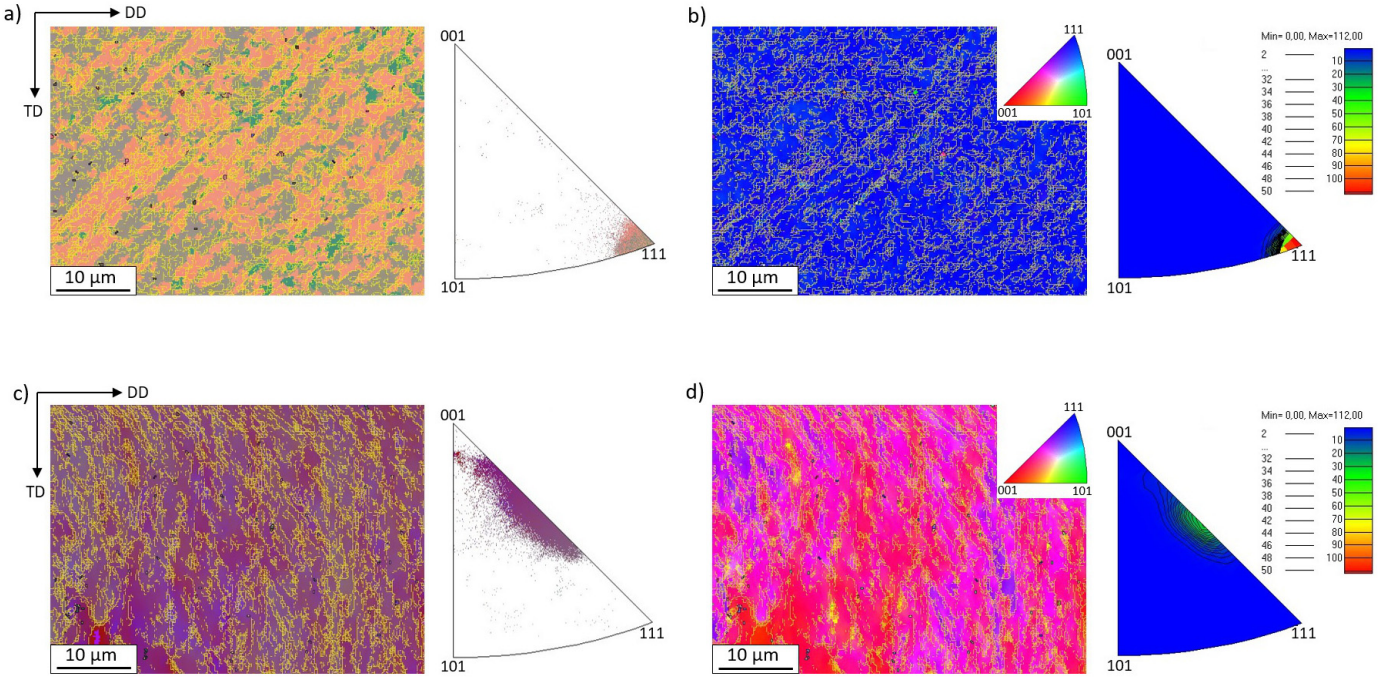

Fig. 5. The EBSD results presented by: a,c) the maps of all Euler angles and their corresponding inverse pole figures and b,d) the precession diffraction orientation map with color code as an inset for samples: a,b) Cu <111> and c,d) Cu <001>, respectively

defined by Chen et al., when the strain generated during the cold drawing process is greater than 1.96, the orientation of <111> is more stable than <001> during deformation [8]. Examinations of Cu <001> show the presence of multiple counts of orientations between the main directions <111> and <001> (Fig. 5c and d – IPFs), which testifies to the blurred local texture. This phenomenon can be explained by noting the formation of shear bands in the TEM images in Fig. 3a and b, and this may lead to scattering of the material texture [38]. Presented at the Fig. 5 maps of all Euler angles for investigated samples contains the low angle grain boundaries (with a disorientation angle <15°) and high angle grain boundaries (disorientation angle >15°) marked as yellow and black, respectively. In both samples, a slight disorientation of the analyzed microstructures is visible, which indicates that the dominant share is comprised of low angle boundaries, which is typical for dislocation structures.

Electrochemical testing of Cu <111> and Cu <001> was conducted in 3.5 wt.% NaCl, and the results are presented in Figs 6-9.

In Fig. 6, potential evaluation measured in an open circuit (E_{OCP}) by immersing the samples for 30 min in 3.5 wt.% NaCl was not stable for the entire immersion time. In the beginning, a fast decline of E_{OCP} was registered for Cu <001>, and then after nearly 3 min, the E_{OCP} levelled off around –212 mV. A slightly lower E_{OCP} was obtained for Cu <111>, and the E_{OCP} value continually decreased. The observed E_{OCP} oscillations are related to anodic and cathodic reactions that occurred on the surfaces of the examined samples.

Representative electrochemical impedance spectroscopy results are shown in Fig. 7 as Nyquist and Bode plots, which were fitted with equivalent circuits shown in Fig. 8. The presented Nyquist plots may have two overlapped capacitive semicircles, thus the equivalent circuit with two times constant was used for fitting [12,46,47]. Herein, the R_s is the solution resistance, and R_f is the resistance of the film formed on the copper surface. The constant phase element (*CPE*) is typically used to describe non-ideal capacitive behavior due to uneven current distribution or surface inhomogeneity. In the presented equivalent circuit, there is also R_{ct}, which describes the double layer charge transfer resistance, and CPE_{dl}, which is the capacitance of a double layer. For Cu <001>, a straight tail was observed in the low-frequency region of the Nyquist plot, which is attributed to Warburg impedance (marked as *W* on the equivalent circuit shown in Fig. 8b) [46,48,49]. The fitting results are presented in Tab. 1.

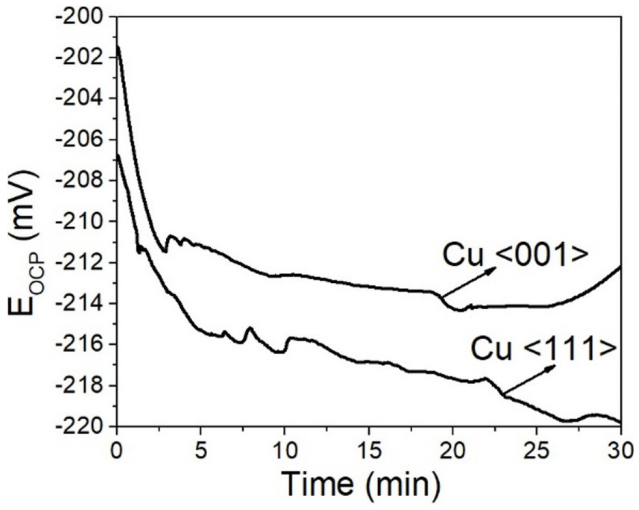

Fig. 6. EOCP evaluation over 30 min of samples' immersion in 3.5 wt. %. NaCl at ambient temperature obtained for Cu <111> and Cu <001>

Based on the Nyquist plots presented in Fig. 7a, the semicircles in the high and middle frequency regions are depressed for both Cu samples. As the fitted results show, the R_{ct} value obtained for Cu <111> is almost twice as high as Cu <001>, with values of 10526 and 5081 $\Omega \cdot cm^2$, respectively. The corrosion mechanism of Cu <001> is controlled by a diffusion process rather than a charge transfer process. This is confirmed by the Warburg impedance which has occurred in the low-frequency region of the Nyquist plot for Cu <001> and is also verified by the phase angle shift from higher to lower frequency (Fig. 7c). As commonly described, this can be attributed to the anodic diffusion of $CuCl_2$ from the surface of the electrode to the solution [48,50], or to the cathodic diffusion of dissolved oxygen from the bulk solution to the surface of examined material [51]. In addition to the two different corrosion mechanisms, the total impedance modulus in the low-frequency range for Cu <001> (~8000 $A \cdot cm^2$) was two-times higher than that of Cu <111> (~4000 $A \cdot cm^2$) (Fig. 7b). This indicates that Cu <111> is more active than Cu <001> in the analyzed corrosive medium.

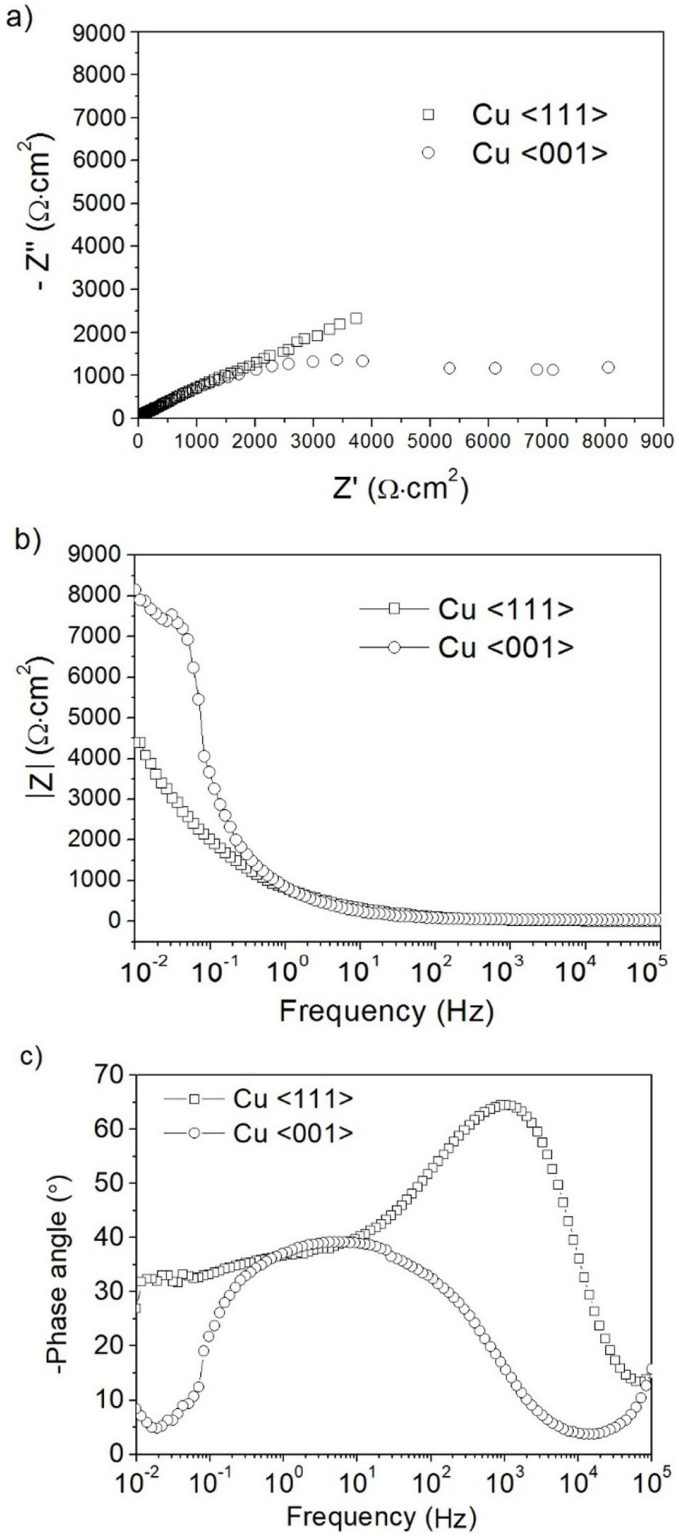

Fig. 7. EIS spectra obtained for analyzed materials a) Nyquist plots, b) and c) Bode plots where b) represents the total impedance versus frequency and c) shows the phase angle versus frequency

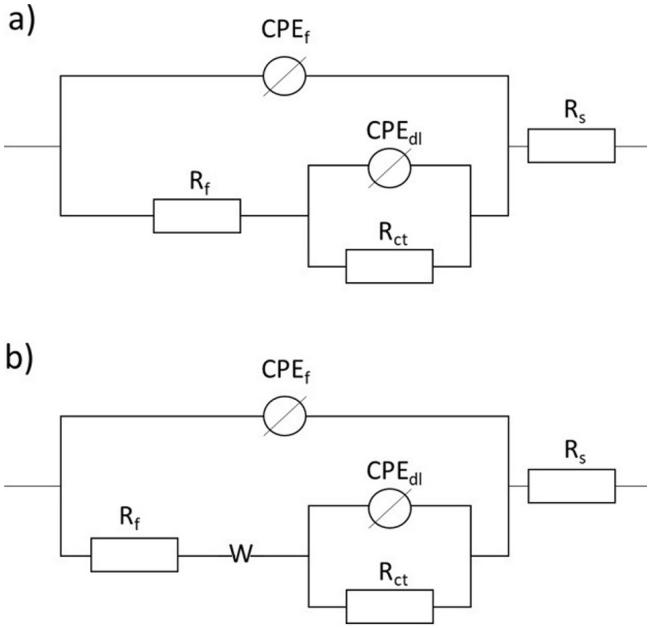

Fig. 8. Equivalent electric circuits used for fitting EIS results for: a) Cu <111>; b) Cu <001>

Figure 9 presents the anodic polarization curves of Cu <111> and Cu <001> in 3.5 wt.% NaCl fitted via Tafel extrapolation method, and the resulting basic electrochemical parameters are presented in Tab. 2. The shape of each polarization curve is different, and the Cu <001> polarization curve shows a slightly lower current density range than the polarization curve of Cu <111>. This shows that in 3.5 wt.% NaCl, Cu <001> corrodes more slowly than Cu <111>. Based on the Tafel extrapolation results, the corrosion current density (i_{corr}) calculated for Cu <111> is around 2.2 $mA \cdot cm^{-2}$, which is nearly two times higher than i_{corr} (1.4 $mA \cdot cm^{-2}$) obtained for Cu <001>. A lower E_{corr} was obtained for Cu <111> than for Cu <001> (–251 mV and –174 mV, respectively). The higher current density range and higher i_{corr} suggest that Cu <111> is less resistant in the analyzed medium than Cu <001>. On the Cu <001> surface, a corrosion product film formed, and a breakdown potential (E_b) is observed (E_b = –96 mV).

SEM in SE (secondary electrons) observations on a cross-section perpendicular to the drawing direction of the examined Cu sample surfaces indicate significant differences in their ap-

TABLE 1

Fitting results obtained with equivalent circuits presented in Fig. 8; R_s – solution resistance, R_f – film resistance, R_{ct} – charge transfer resistance, CPE_f – constatnt phase element of film, a_f – parameter of CPE_f, CPE_{dl} – constatnt phase element of double layer, a_{dl} – parameter of CPE_{dl}, w – Warburg impedance parameter

Samples	R_s [Ω·cm^2]	R_f [Ω·cm^2]	R_{ct} [Ω·cm^2]	CPE_f [μF·cm^{-2}]	a_f	CPE_{dl} [μF·cm^{-2}]	a_{dl}	w
Cu <111>	3.4	45.6	10526	8	0.99	500	0.44	—
Cu <001>	13	44	5081	0.001	0.69	409	0.51	0.00014

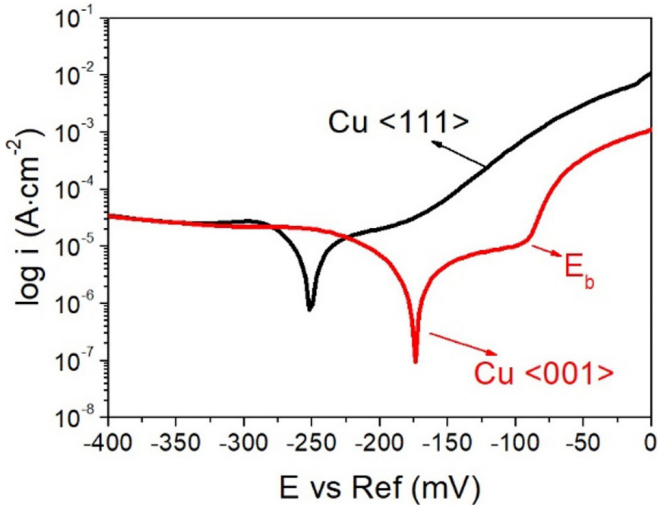

Fig. 9. Potentiodynamic polarization curves obtained for Cu <111> and Cu <001> in 3.5 wt.% NaCl after 30 min of immersion in OCP

TABLE 2

Basic electrochemical parameters obtained from PDP by Tafel extrapolation method; E_{corr} – corrosion potential, i_{corr} – corrosion current density, E_b – breakdown potential

Material	E_{corr} (mV vs Ref)	i_{corr} (mA·cm^{-2})	E_b (mV vs Ref)
Cu <001>	–174	1.4	–96
Cu <111>	–251	2.2	—

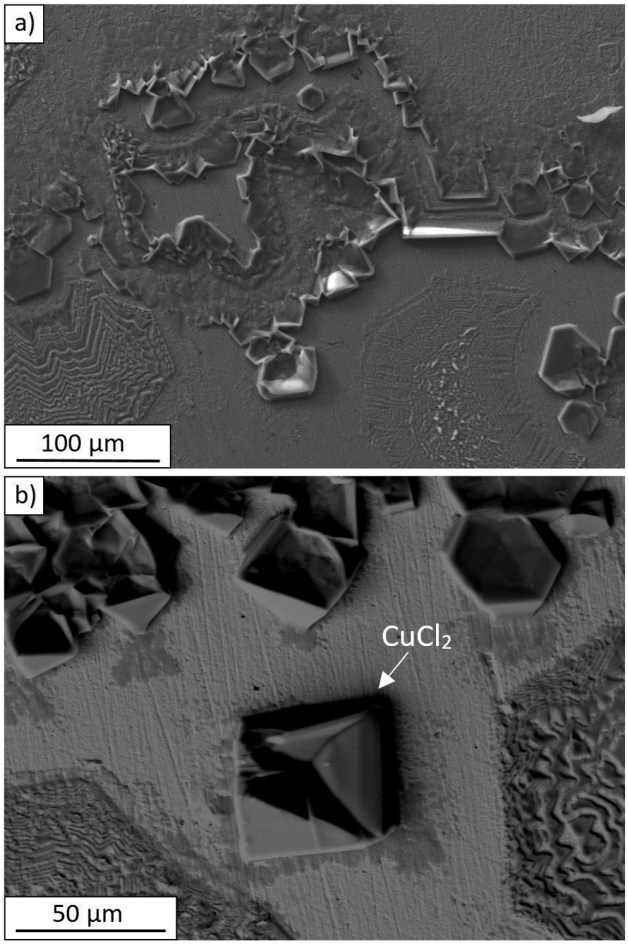

Fig. 10. SEM Surface observations after electrochemical measurements in 3.5 wt.% NaCl obtained for Cu <111>

pearance (Figs 10 and 11). The formation of a layer of early-stage corrosion products is observed for Cu <111> (Fig. 10a), whose surface is covered with non-uniformly-distributed corrosion products, which are cubic in shape (Fig. 10b). These features can be identified as soluble $CuCl_2$ [52], which may enhance Cu corrosion in the solution containing chloride ions [53,54]. The surface of Cu <001> is uniformly covered with an oxide layer, which forms a compact film on the examined surface of the sample. Dissolution of the oxide layer occurred at grain boundaries (Fig. 11a and b), which is also confirmed by the E_b observed at the anodic branch of the polarization curve obtained for Cu <001> (Fig. 10).

The corrosion behavior of the examined materials is strongly dependent on its final microstructure and texture evolution. As the electrochemical data showed, the corrosion mechanisms of Cu <111> were controlled by double charge transfer processes, whilst mixed diffusive and charge transfer processes occurred for Cu <001>. The surface of Cu <001> was covered with a homogeneous, compact oxide layer, which improved its resistivity in 3.5 wt.% NaCl. Cu <111> was more active in the tested solution, where a sharper texture was observed.

It has been previously shown that the corrosion behavior of polycrystalline fcc metals is correlated with surface energy, which has been calculated by Fu et al. [55] and Wen et al. [56]. They defined that grains oriented in the <111> direction have lower surface energies than those oriented in the <001> direction. In this work, the predominant orientation of grains in Cu <111> were consistent with the initial orientation of single crystal, and in the Cu <001> sample, the structure was dispersed around the <001> orientation. Therefore, it can be assumed that the Cu <001> more easily formed a compact oxide layer than Cu <111>. This confirms that the formation of a stable Cu_2O layer on the surface of the Cu <001> was much more favorable.

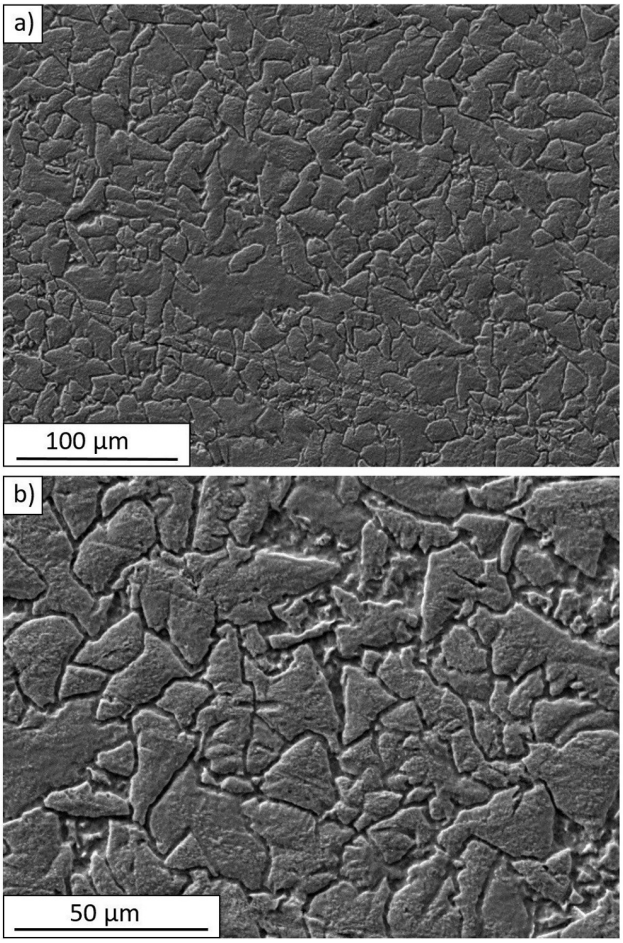

Fig. 11. SEM Surface observations after electrochemical measurements in 3.5 wt.% NaCl obtained for Cu <001>

The role of a Cu_2O layer in the corrosion of drawn Cu has been previously investigated by Ogata et al. [57] who stated that an oxide layer was formed in polycrystalline Cu wires on grains oriented in the <001> direction. It is commonly known that the Cu_2O layer formed during Cu corrosion plays an important role and can separate bulk materials from a corrosive solution. Thus, corrosive reactions on grain surfaces dispersed around the <001> orientation were much slower than the reactions on grains which were primarily oriented at components close to <111>. Therefore, the surface corrosion of the Cu <111> sample was strongly accelerated by Cl^-, which is confirmed by the presence of the soluble $CuCl_2$ which adsorbed on the surface of Cu <111>.

Thus, the results described in this work suggest that the corrosion behavior of the analyzed materials was also influenced by factors other than the grain orientation. On the surface of Cu <001>, a compact layer of corrosion products formed, which dissolved at grain boundaries. This suggests it is strongly associated with a higher dislocation density, which is determined by the formation of dislocation cells. In addition, XRD and EBSD measurements showed a weaker texture for material in this state, which increased the disorientation of grain boundaries and affected the corrosion resistance of the Cu <001> sample.

Further research should be conducted to investigate different dislocation structures or grain orientations and their respectively different potentials and the possibility of forming anodic-cathodic couples responsible for the electrochemical activity of Cu. This can also have a strong effect on the protective ability of the formed oxide layer.

4. Conclusions

Based on the results presented in this work, the following conclusions can be drawn:

1. Due to the cold drawing process, strongly-developed substructures with many dislocations were obtained for Cu single crystals with an initial orientation of <111>. In the Cu single crystals with an initial orientation of <001>, the formation of dislocation cell structures and shear bands was visible, which increased the grain disorientation and weakened the texture.
2. The corrosion resistance of drawn Cu single crystals with initial orientations of <111> and <001> was strongly dependent on the materials' initial orientation. Different volumes of texture components dominated the present materials during the electrochemical testing of corrosion reactions. The corrosion of the drawn Cu single crystal with an initial orientation of <111> was controlled by reactions occurring at the double layer, whilst for drawn Cu single crystal with an initial orientation of <001>, the corrosion was controlled by diffusion.
3. Drawn Cu single crystal with an initial orientation of <001> was more resistive in 3.5 wt.% NaCl, than the material initially oriented at <111>. The improved resistance to corrosive reactions is due to the formation of an oxide layer.

Acknowledgments

This work was supported by The National Science Center of Poland (project no: 2016/21/B/ST8/01183) „The influence of orientation of single crystals with different stacking fault energy on deformation texture formation during drawing".

REFERENCES

[1] N. Al-Araji, M.A.-T. Haydar, T.A. Wissam, The role of cold drawing on electrical and mechanical properties of copper the role of cold drawing on electrical and mechanical properties of copper cables, Int. J. Adv. Technol. Eng. Explor. **2**, 2394-7454 (2018).

[2] K.S. Kim, J.Y. Song, E.K. Chung, J.K. Park, S.H. Hong, Relationship between mechanical properties and microstructure of ultra-fine gold bonding wires, Mech. Mater. **38**, 119-127 (2006) DOI:10.1016/j.mechmat.2005.05.015.

[3] J. Chen, W. Yan, B. Li, X.G. Ma, X.Z. Du, X.H. Fan, Microstructure and texture evolution of cold drawing (111) single crystal copper, Sci. China Technol. Sci. **54**, 1551-1559 (2011) DOI:10.1007/s11431-011-4349-5.

[4] K. Rajan, R. Petkie, Microtexture and anisotropy in wire drawn copper, Mater. Sci. Eng. A. **257**, 185-197, (1998) DOI:10.1016/S0921-5093(98)00838-7.

[5] H.-J. Shin, H.-T. Jeong, D.N. Lee, Deformation and annealing textures of silver wire, Mater. Sci. Eng. A **279**, 244-253, (2002) DOI:10.1016/s0921-5093(99)00535-3.

[6] S.G. Chowdhury, S. Das, P.K. De, Cold rolling behaviour and textural evolution in AISI 316L austenitic stainless steel, Acta Mater. **53**, 3951-3959 (2005) DOI:10.1016/j.actamat.2005.05.006.

[7] A.T. English, G.Y. Chin, On the variation of wire texture with stacking fault energy in f.c.c. metals and alloys, Acta Metall. **13**, 1013-1016 (1965) DOI:10.1016/0001-6160(65)90010-6.

[8] J. Chen, X.H. Fan, C.X. Liu, D.R.G., X. Fan, Dependence of texture evolution on initial orientation in drawn single crystal copper, Mater. Charact. **62**, 237-242 (2011) DOI:10.1016/j.matchar.2010.12.006.

[9] E.J. Palmiere, B.P. Wynne, L. Sun, W.M. Rainforth, P. Gong, The effect of thermomechanical controlled processing on recrystallisation and subsequent deformation-induced ferrite transformation textures in microalloyed steels, J. Mater. Sci. **53**, 6922-6938 (2018) DOI:10.1007/s10853-018-2029-6.

[10] N. Jia, D. Raabe, X. Zhao, Texture and microstructure evolution during non-crystallographic shear banding in a plane strain compressed Cu-Ag metal matrix composite, Acta Mater. **76**, 238-251 (2014) DOI:10.1016/j.actamat.2014.05.036.

[11] L. Lapeire, E. Martinez Lombardia, K. Verbeken, I. De Graeve, L.A.I. Kestens, H. Terryn, Effect of neighboring grains on the microscopic corrosion behavior of a grain in polycrystalline copper, Corros. Sci. **67**, 179-183 (2013) DOI:10.1016/j.corsci.2012.10.017.

[12] K. Rahmouni, M. Keddam, A. Srhiri, H. Takenouti, Corrosion of copper in 3% NaCl solution polluted by sulphide ions, Corros. Sci. **47**, 3249-3266 (2005) DOI:10.1016/j.corsci.2005.06.017.

[13] Y. Ein-Eli, D. Starosvetsky, Review on copper chemical-mechanical polishing (CMP) and post-CMP cleaning in ultra large system integrated (ULSI)-An electrochemical perspective, Electrochim. Acta. **52**, 1825-1838 (2007) DOI:10.1016/j.electacta.2006.07.039.

[14] Z.Y. Chen, S. Zakipour, D. Persson, C. Leygraf, Effect of sodium chloride particles on the atmospheric corrosion of pure copper, Corros. Sci. **60**, 479-491 (2004) DOI:10.5006/1.3299244.

[15] J.P. Franey, M.E. Davis, Metallographic studies of the copper patina formed in the atmosphere, Corros. Sci. **27**, 659-668 (1987) DOI:10.1016/0010-938X(87)90048-5.

[16] R.L. Frost, Raman spectroscopy of selected copper minerals of significance in corrosion, Spectrochim. Acta – Part A Mol. Biomol. Spectrosc. **59**, 1195-1204 (2003) DOI:10.1016/S1386-1425(02)00315-3.

[17] M. Metikoš-Huković, I. Škugor, Z. Grubač, R. Babić, Complexities of corrosion behaviour of copper-nickel alloys under liquid impingement conditions in saline water, Electrochim. Acta. **55**, 3123-3129 (2010) DOI:10.1016/j.electacta.2010.01.066.

[18] J.M. Bastidas, E. Cano, D.M. Bastidas, S. Fajardo, M. Criado, V.M. La Iglesia, Copper deterioration: causes, diagnosis and risk minimisation, Int. Mater. Rev. **55**, 99-127 (2010) DOI:10.1179/095066009x12506721665257.

[19] M. Ochoa, M.A. Rodríguez, S.B. Farina, Corrosion of high purity copper in solutions containing NaCl , Na 2 SO 4 and NaHCO 3 at different temperatures, Procedia Mater. Sci. **9**, 460-468 (2015) DOI:10.1016/j.mspro.2015.05.017.

[20] S.A. Kaluzhina, I.V. Kobanenko, Mechanism of local activation of copper in the presence of chloride and sulfate ions at elevated temperature and heat transfer, Prot. Met. **37**, 237-243 (2001) DOI:10.1023/A:1010494226972.

[21] L. Lapeire, Influence of grain size on the electrochemical behavior of pure copper, J. Mater. Sci. **52**, 1501-1510 (2017) DOI:10.1007/s10853-016-0445-z.

[22] S.S. Kim, U. Erb, K. Aust, G. Palumbo, Grain boundary character distribution and intergranular corrosion in high-purity aluminum, Scr. Mater. **44**, 835-839 (2001) DOI:10.1016/S1359-6462(00)00682-5.

[23] H. Chen, M. Bettayeb, V. Maurice, L.H. Klein, L. Lapeire, K. Verbeken, et al., Local passivation of metals at grain boundaries: In situ scanning tunneling microscopy study on copper, Corros. Sci. **111**, 659-666, (2016) DOI:10.1016/j.corsci.2016.04.013.

[24] H. Miyamoto, K. Ikeuchi, T. Mimaki, The role of grain boundary plane orientation on intergranular corrosion of symmetric and asymmetric [1 1 0] tilt grain boundaries in directionally solidified pure copper, Scr. Mater. **50**, 1417-1421, (2004) DOI:10.1016/j.scriptamat.2004.03.016.

[25] K. Hagihara, M. Okubo, M. Yamasaki, T. Nakano, Crystal-orientation-dependent corrosion behaviour of single crystals of a pure Mg and Mg-Al and Mg-Cu solid solutions, Corros. Sci. **109**, 68-85, (2016) DOI:10.1016/j.corsci.2016.03.019.

[26] G.L. Song, R. Mishra, Z. Xu, Crystallographic orientation and electrochemical activity of AZ31 Mg alloy, Electrochem. Commun. (2010) DOI:10.1016/j.elecom.2010.05.011.

[27] M. Liu, D. Qiu, M.C. Zhao, G. Song, A. Atrens, The effect of crystallographic orientation on the active corrosion of pure magnesium, Scr. Mater. **58**, 421-424 (2008) DOI:10.1016/j.scriptamat.2007.10.027.

[28] G.K. Williamson, W. Hall, X-ray line boradening from filed aluminium and wolfram, Acta Metall. **1**, 22-30 (1953) DOI:10.1016/0001-6160(53)90006-6.

[29] J. Han, Z. Zhu, H. Li, C. Gao, Microstructural evolution, mechanical property and thermal stability of Al-Li 2198-T8 alloy processed by high pressure torsion, Mater. Sci. Eng. A. **651**, 435-441 (2016) DOI:10.1016/j.msea.2015.10.112.

[30] I.F. Mohamed, Y. Yonenaga, S. Lee, K. Edalati, Z. Horita, Age hardening and thermal stability of Al-Cu alloy processed by high-pressure torsion, Mater. Sci. Eng. A **627**, 111-118 (2015) DOI:10.1016/j.msea.2014.12.117.

[31] W. Brandt, R. Paulin, C. Dauwe, Positron trapping by defects in plastically deformed copper, Phys. Lett. A **48**, 480-482 (1974) DOI:10.1016/0375-9601(74)90632-X.

[32] L.G. Schulz, A direct method of determining preferred orientation of a flat reflection sample using a geiger counter x-ray spectrometer, J. Appl. Phys. **20**, 1030-1033 (1949) DOI:10.1063/1.1698268.

[33] T. Wejrzanowski, W.L. Spychalski, K. Rożniatowski, K.J. Kurzydłowski, Image based analysis of complex microstructures of

engineering materials, Int. J. Appl. Math. Comput. Sci. **18**, 33-39 (2008) DOI:10.2478/v10006-008-0003-1.

[34] P. Li, Z.F. Zhang, X.W. Li, S.X. Li, Z.G. Wang, Effect of orientation on the cyclic deformation behavior of silver single crystals: Comparison with the behavior of copper and nickel single crystals, Acta Mater. **57**, 4845-4854 (2009) DOI:10.1016/j.actamat.2009.06.048.

[35] P. Li, S.X. Li, Z.G. Wang, Z.F. Zhang, Fundamental factors on formation mechanism of dislocation arrangements in cyclically deformed fcc single crystals, Prog. Mater. Sci. **56**, 328-377 (2011) DOI:10.1016/j.pmatsci.2010.12.001.

[36] H. Paul, J.H. Driver, Z. Jasieński, Shear banding and recrystallization nucleation in a Cu-2% Al alloy single crystal, Acta Mater. **50**, 815-830 (2002) DOI:10.1016/S1359-6454(01)00381-0.

[37] H. Paul, J.H. Driver, C. Maurice, A. Piatkowski, The role of shear banding on deformation texture in low stacking fault energy metals as characterized on model Ag crystals, Acta Mater. **55**, 575-588, (2007) DOI:10.1016/j.actamat.2006.08.051.

[38] P. Eisenlohr, F. Roters, D. Raabe, X. Zhao, N. Jia, Orientation dependence of shear banding in face-centered-cubic single crystals, Acta Mater. **60**, 3415-3434 (2012) DOI:10.1016/j.actamat.2012.03.005.

[39] L.A.I. Kestens, H. Pirgazi, Texture formation in metal alloys with cubic crystal structures, Mater. Sci. Technol. (United Kingdom). **32**, 1303-1315, (2016) DOI:10.1080/02670836.2016.1231746.

[40] X. Huang, G. Winther, Dislocation structures. Part I. Grain orientation dependence, Philos. Mag. **87**, 5189-5214, (2007) DOI:10.1080/14786430701652851.

[41] M. Odnobokova, A. Belyakov, R. Kaibyshev, Grain refinement and strengthening of austenitic stainless steels during large strain cold rolling, Philos. Mag. **99**, 531-556 (2018) DOI:10.1080/14786435.2018.1546961.

[42] C. Haase, S.G. Chowdhury, L.A. Barrales-Mora, D.A. Molodov, G. Gottstein, On the relation of microstructure and texture evolution in an austenitic Fe-28Mn-0.28C TWIP steel during cold rolling, Metall. Mater. Trans. A Phys. Metall. Mater. Sci. **44**, 911-922 (2013) DOI:10.1007/s11661-012-1543-4.

[43] Z. Yanushkevich, A. Belyakov, C. Haase, D.A. Molodov, R. Kaibyshev, Structural/textural changes and strengthening of an advanced high-Mn steel subjected to cold rolling, Mater. Sci. Eng. A **651**, 763-773 (2016) DOI:10.1016/j.msea.2015.11.027.

[44] X.H. Fan, D. Tang, W.L. Fang, D.Y. Li, Y.H. Peng, Microstructure development and texture evolution of aluminum multi-port extrusion tube during the porthole die extrusion, Mater. Charact. **118**, 468-480 (2016) DOI:10.1016/j.matchar.2016.06.025.

[45] F. Pérocheau, J.H. Driver, Texture gradient simulations for extrusion and reversible rolling of FCC metals, Int. J. Plast. **16**, 73-89 (2000) DOI:10.1016/S0749-6419(99)00048-0.

[46] S. Chen, D. Zhang, Study of corrosion behavior of copper in 3.5/wt.% NaCl solution containing extracellular polymeric substances of an aerotolerant sulphate-reducing bacteria, Corros. Sci. **136**, 275-284 (2018) DOI:10.1016/j.corsci.2018.03.017.

[47] D. Wang, B. Xiang, Y. Liang, S. Song, C. Liu, Corrosion control of copper in 3.5 wt.% NaCl solution by domperidone: Experimental and theoretical study, Corros. Sci. **85**, 77-86 (2014) DOI:10.1016/j.corsci.2014.04.002.

[48] W. Chen, S. Hong, H.B. Li, H.Q. Luo, M. Li, N.B. Li, Protection of copper corrosion in 0.5M NaCl solution by modification of 5-mercapto-3-phenyl-1,3,4-thiadiazole-2-thione potassium self-assembled monolayer, Corros. Sci. **61**, 53-62 (2012) DOI:10.1016/j.corsci.2012.04.023.

[49] T. Kosec, Z. Qin, J. Chen, A. Legat, D.W. Shoesmith, Copper corrosion in bentonite/saline groundwater solution: Effects of solution and bentonite chemistry, Corros. Sci. **90**, 248-258 (2015) DOI:10.1016/j.corsci.2014.10.017.

[50] S.L. Li, Y.G. Wang, S.H. Chen, R. Yu, S.B. Lei, H.Y. Ma et al., Some aspects of quantum chemical calculations for the study of Schiff base corrosion inhibitors on copper in NaCl solutions, Corros. Sci. **41**, 1769-1782 (1999) DOI:10.1016/S0010-938X(99)00014-1.

[51] Y. Feng, K.-S. Siow, W.-K. Teo, K.-L. Tan, A.-K. Hsieh, Synergistic effects between sodium tripolyphosphate and zinc sulfate in corrosion inhibition for copper in neutral tap water, Corrosion. **53**, 546-555 (1997) DOI:10.5006/1.3290286.

[52] E.M. Sherif, Corrosion behavior of copper in 0 . 50 M hydrochloric acid pickling solutions and its inhibition by 3-amino-1,2,4-triazole, Corrosion. **7**, 1884-189 (2012).

[53] C. Lilja, S. Engström, O. Olsson, A. Hedin, A. Ström, Influence of high chloride concentration on copper corrosion, SKM Memo Publiaction 1-6, (2013).

[54] H. Zhao, J. Chang, A. Boika, A.J. Bard, Electrochemistry of high concentration copper chloride complexes, Anal. Chem. **85**, 7696–7703, (2013) DOI:10.1021/ac4016769.

[55] B. Fu, W. Liu, Z. Li, Calculation of the surface energy of fcc-metals with the empirical electron surface model, Appl. Surf. Sci. **256**, 6899-6907 (2010) DOI:10.1016/j.apsusc.2010.04.108.

[56] Y.N. Wen, J.M. Zhang, Surface energy calculation of the fcc metals by using the MAEAM, Solid State Commun. **144**, 163-167 (2007) DOI:10.1016/j.ssc.2007.07.012.

[57] S. Ogata, N. Kobayashi, T. Kitagawa, S. Shima, A. Fukunuga, C. Takatoh, et al., Nanoscale corrosion behavior of polycrystalline copper fine wires in dilute NaCl solution investigated by in-situ atomic force microscopy, Corros. Sci. **105**, 177-182 (2016) DOI:10.1016/j.corsci.2016.01.015.